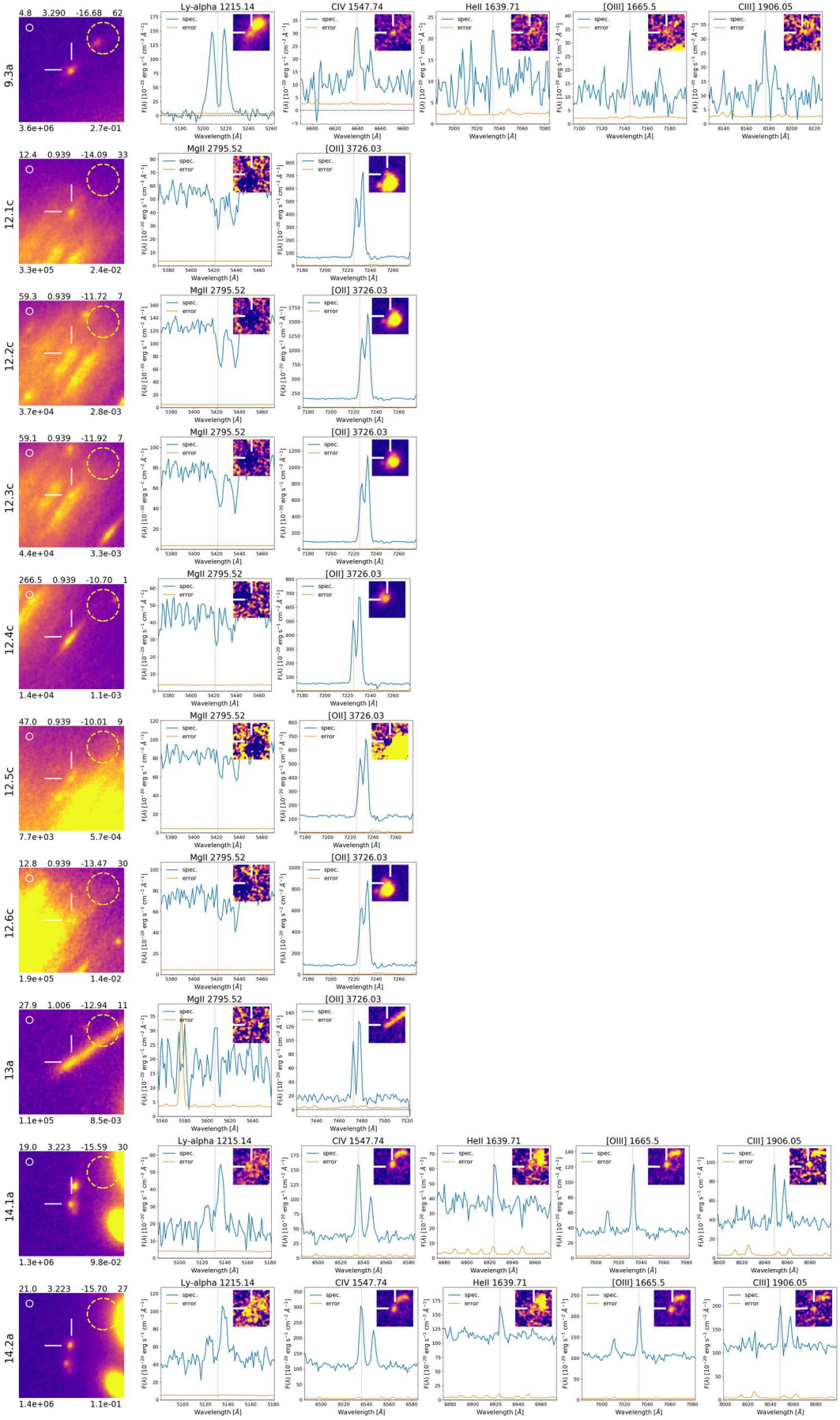

Fig. B.2. continued.

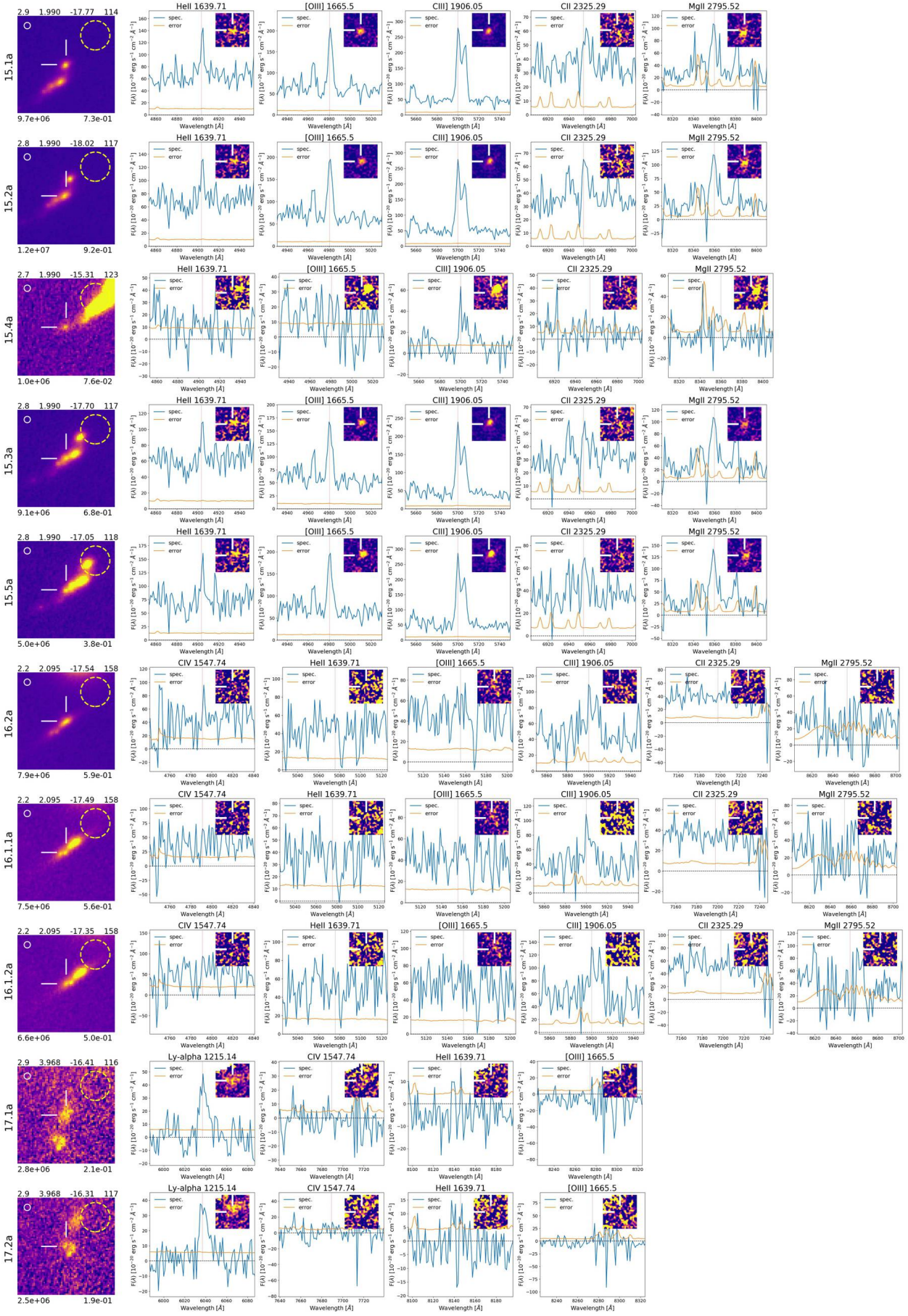

Fig. B.2. continued.

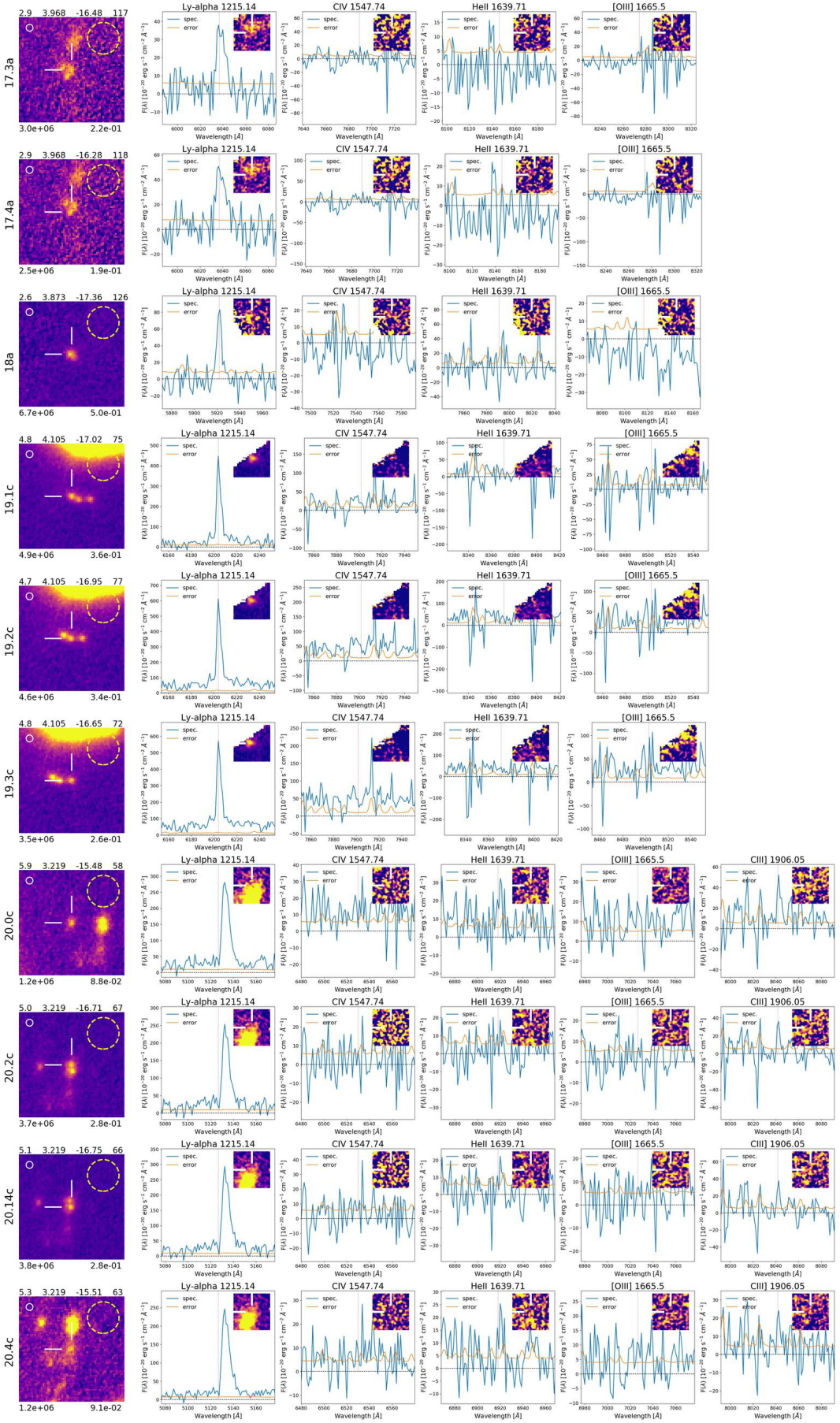

Fig. B.2. continued.

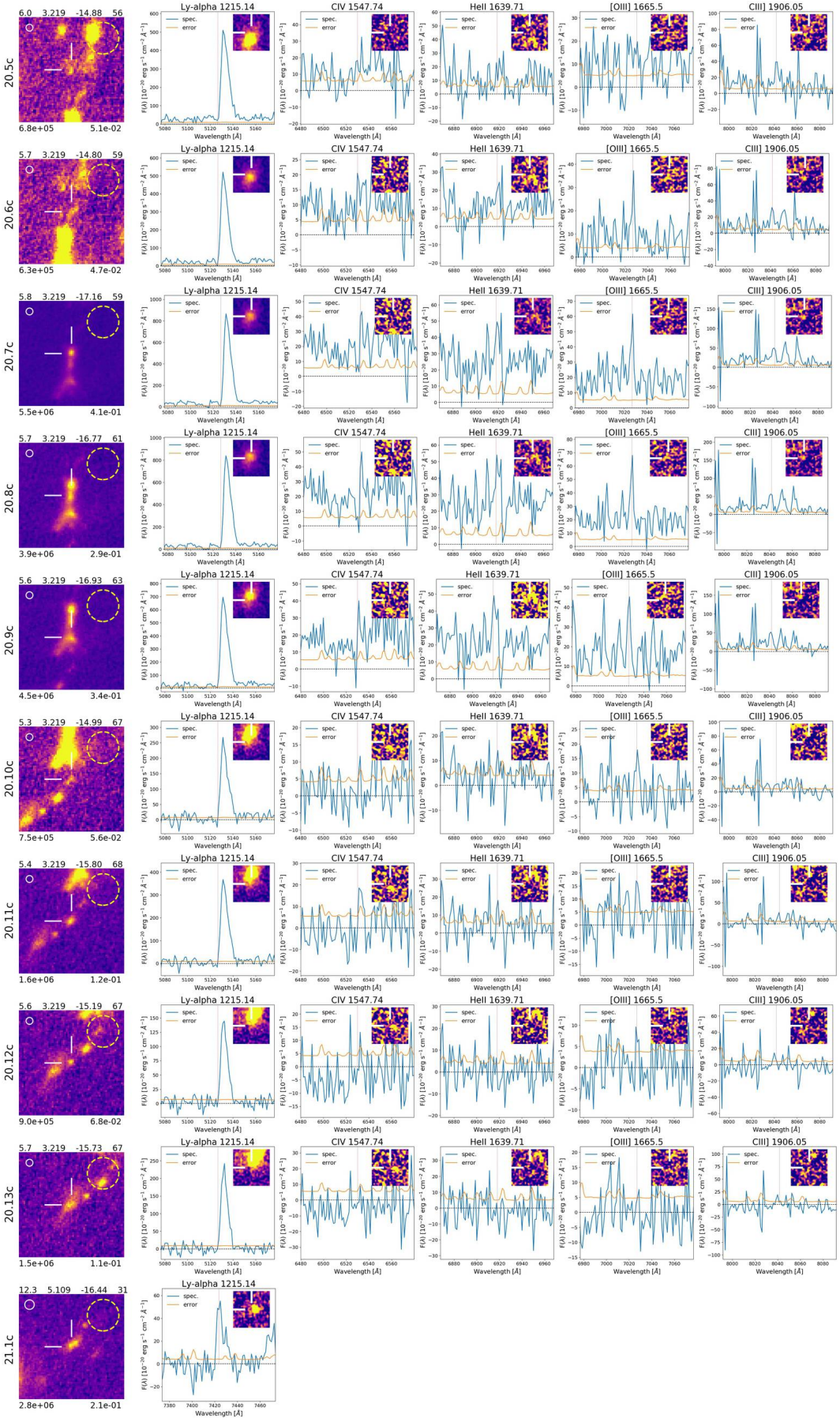

Fig. B.2. continued.

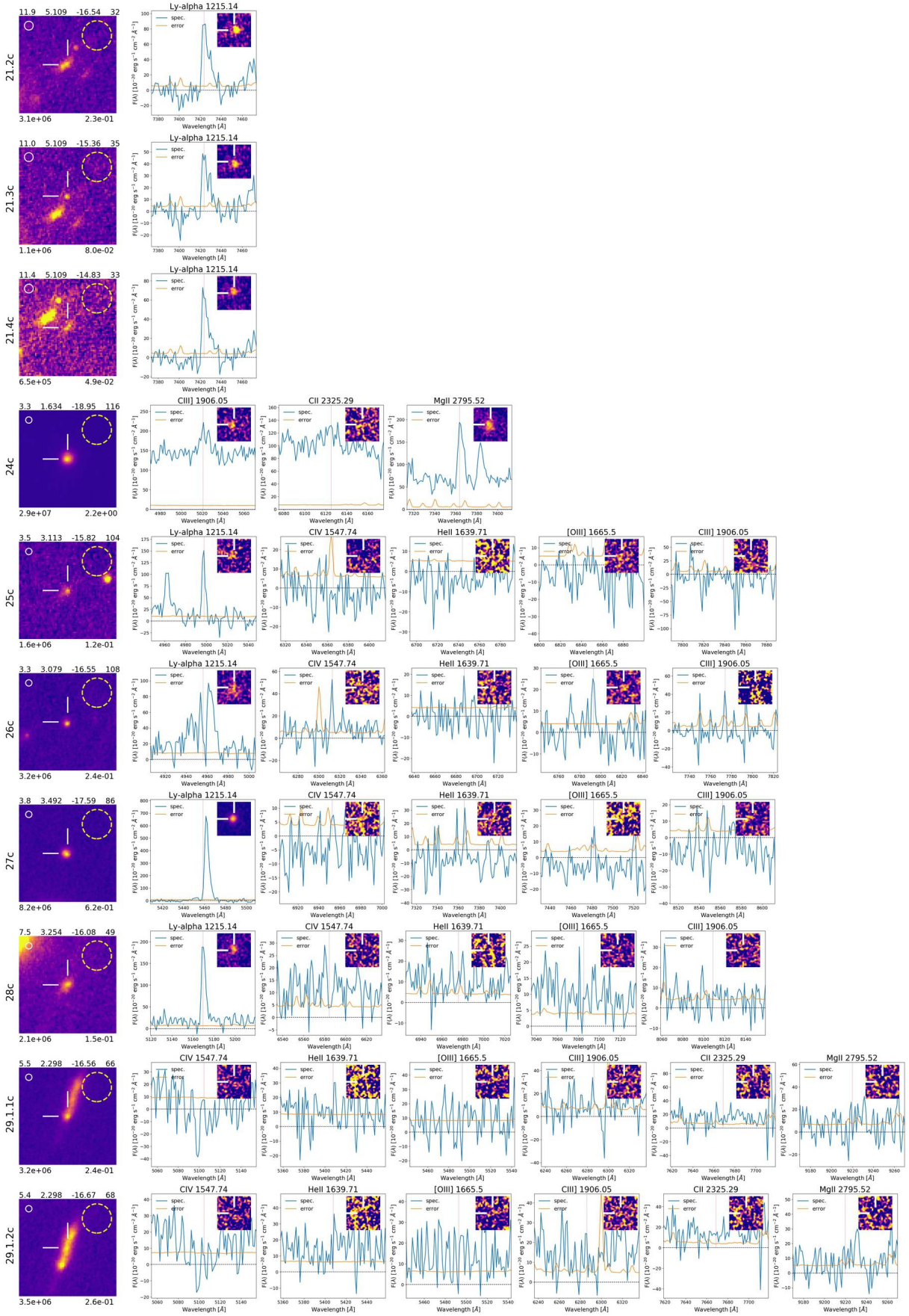

Fig. B.2. continued.

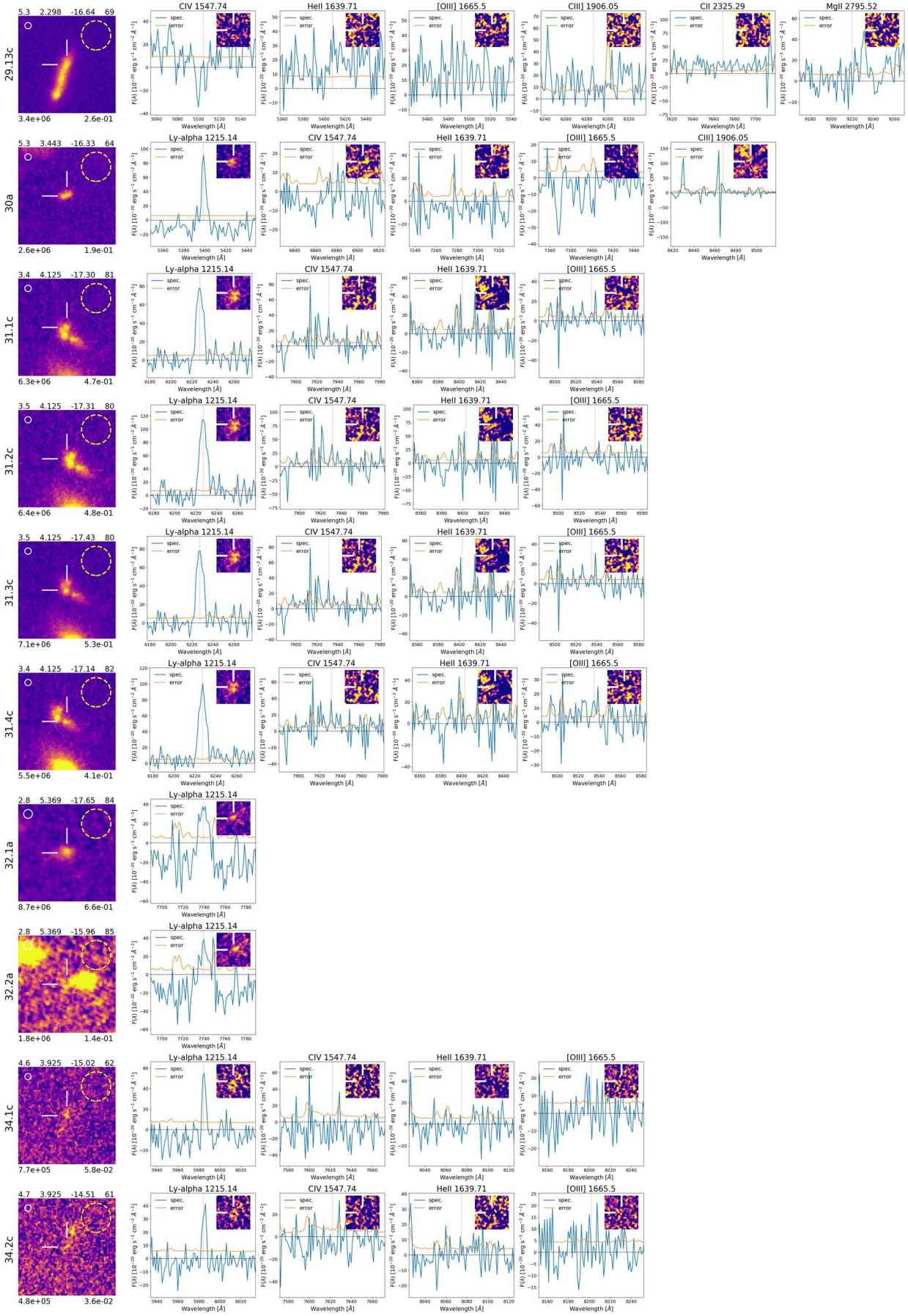

Fig. B.2. continued.

Fig. B.2. continued.

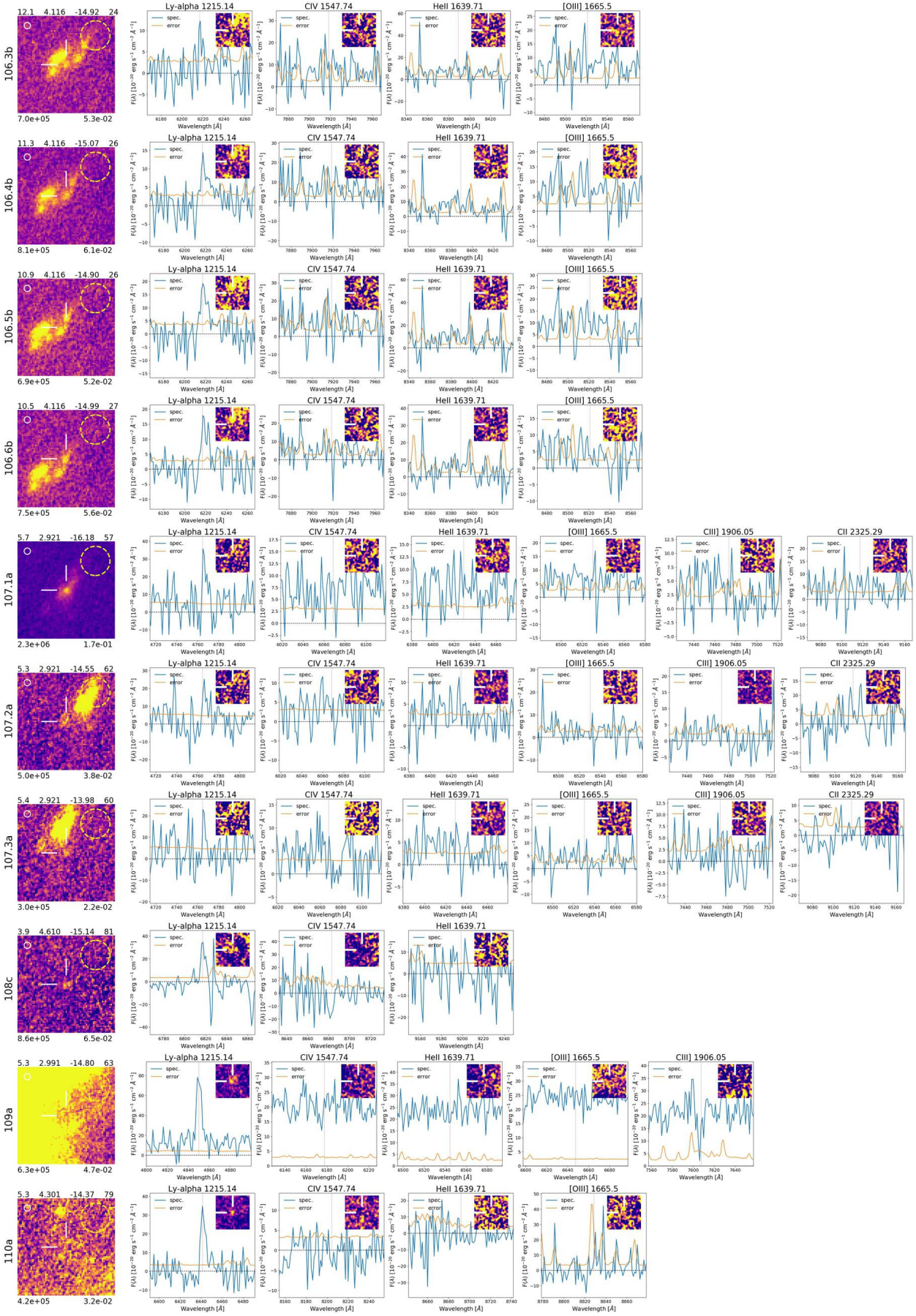

Fig. B.2. continued.

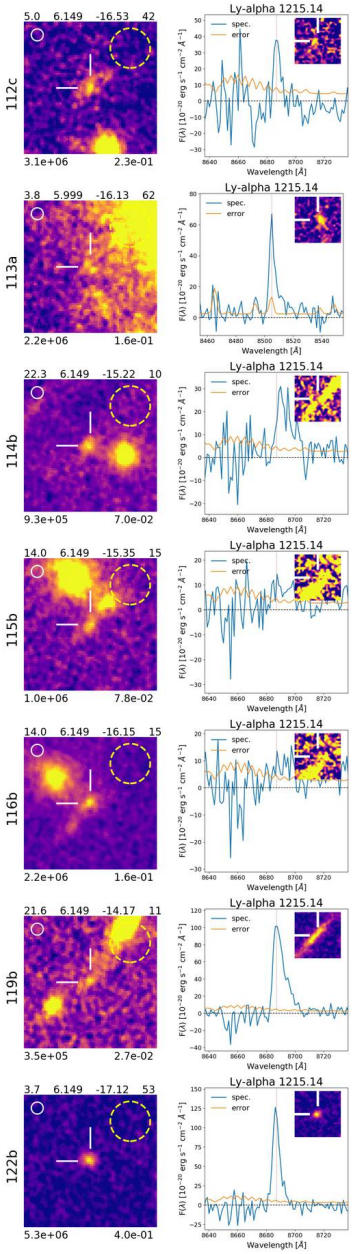

Fig. B.2. continued.

Appendix C: Revisiting magnification for object 14 at $z = 3.223$

Source 14 is split into six multiple images that with the MDLF have now all been confirmed spectroscopically. The new lens model of Bergamini et al. (2021) nicely reproduces the positions of all of them. Here we revisit the magnification initially reported by Vanzella et al. (2017b) and based on the observed flux ratios among the images involved. Indeed, the observed flux ratio among the least and the most magnified images provide a guess of the relative magnification among them (see Appendix E). Under the condition the measured flux is not affected by systematics, it is possible to rescale the more stable predicted magnification of the least magnified image by the observed flux ratio to obtain the magnification of the most magnified one. Vanzella et al. (2017b) did this calculation starting from the least magnified image of source 14 that, however, at that time was not spectroscopically confirmed and was mainly based on the photometric redshift identification (ASTRODEEP, ID = 1141 with magnitude $F814 = 29.1$). With the MDLF we now confirmed the sixth image 14f as ID = 1127, with $F814W = 27.78 \pm 0.07$. The previous wrong identification of image 14f lead to significant overestimations of the magnification value ($\mu \simeq 40$). The inclusion of the correct image 14f (ID = 1127) and after properly computing the rescaling and propagation errors (flux ratio 7.29 ± 0.83 and $\mu(14f) = 2.08 \pm 0.02$), the new value turns out to be $\mu_{\rm tot} = 15.2 \pm 1.7$ for image 14.1b (and similarly for 14.2b). Such a magnification is in line with the estimate provided by the lens model, $\mu_{\rm tot} = 19.4^{+11}_{-5.9}$ (see Table E.1 and Fig. C.1). This fact highlights the importance of having spectroscopically confirmed multiple images.

It is worth mentioning that image ID14f has been confirmed through the detection of CIVλ1548 at $S/N \approx 4$, while Lyα is deficient in this source (as shown in Fig. C.1 and discussed by Vanzella et al. 2017b). Figure C.1 shows such CIV detection for image 14f (the least magnified) and image 14.(1,2)[a,b,c] (the most magnified). For the faintest one (14f), we also calculate the continuum-subtracted weight average of seven narrow-band MUSE images (with dv = 200 km s^{-1}) centered at the position of the ultraviolet transitions CIVλ1548, 1550, HeIIλ1640, OIII]λ1661, 1666, and CIII]$\lambda\lambda$1907, 1909, in which each doublet is resolved and – following the wavelength order – arise from the Carbon, Helium, Oxygen, and Carbon complex (CHOC, 1548, 1550, 1640, 1661, 1666, 1907, 1909), respectively. The weights (that follow the relative line ratios) have been extracted from the mean stacked spectrum reported in Sect. 13. The CHOC ultraviolet signature is detected at $S/N = 6.7$ for image 14f an reaches its peak emission at the systemic redshift (see Appendix C). As discussed in Vanzella et al. (2017b) and shown in Fig. C.1, there is a deficiency of Lyα emission in source 14 (at variance from the typical positive correlation among Lyα equivalent width and ultraviolet CHOC nebular lines, e.g., Feltre et al. 2020). Therefore, without the availability of the rest-frame optical lines (e.g., [OII]λ3727, 3729, [OIII]$\lambda\lambda$4959, 5007, Hβ, Hα) the redshift confirmation for this kind of Lyα-deficient sources is left to high-ionization lines, which, if present (as in the case of source 14 discussed above), can be properly combined to gain in depth through the UV CHOC complex indicator.

From the comparison between the new image 14f and the pair 14.1b−14.2b, it is also possible to set a rough lower limit on the tangential stretch the most magnified images are subjected, 14.1b, 14.2b (or 14.1a, 14.2a). From the lens model of Bergamini et al. (2021), the tangential magnification on image 14f is $\mu_{\rm T} = 1.5 \pm 0.05$ with a small error, being far from the critical lines. Such a value is still too low to make the two knots spatially resolvable with HST imaging (Fig. C.1), implying that the upper limit on the separation among the two on image 14f is not larger than the HWHM (i.e., with a separation of $s_{\rm f} < 0.06''$). On the other hand, the pair 14b (14.1 and 14.2) are well separated by $0.45'' \pm 0.03$, suggesting that the relative tangential magnification is >7.5, and that the tangential one for images 14b is $\mu_{\rm T}(14b) \simeq \mu_{\rm T}(14f) \times 7.5 \gtrsim 11$. This value is in line with the value provided by the lens model (7−20), that, however, is affected by large uncertainties due to the proximity of the objects to the critical lines. Adopting the above estimate of $\mu_{\rm T} > 11$ and the effective radius of $0.045''$ (1.5 ± 0.5 pix) as estimated in Vanzella et al. (2017b), the sizes of each knot of the pair is plausibly smaller than 30 pc, while the two are separated by ∼390 pc in the source plane (Bergamini et al. 2021).

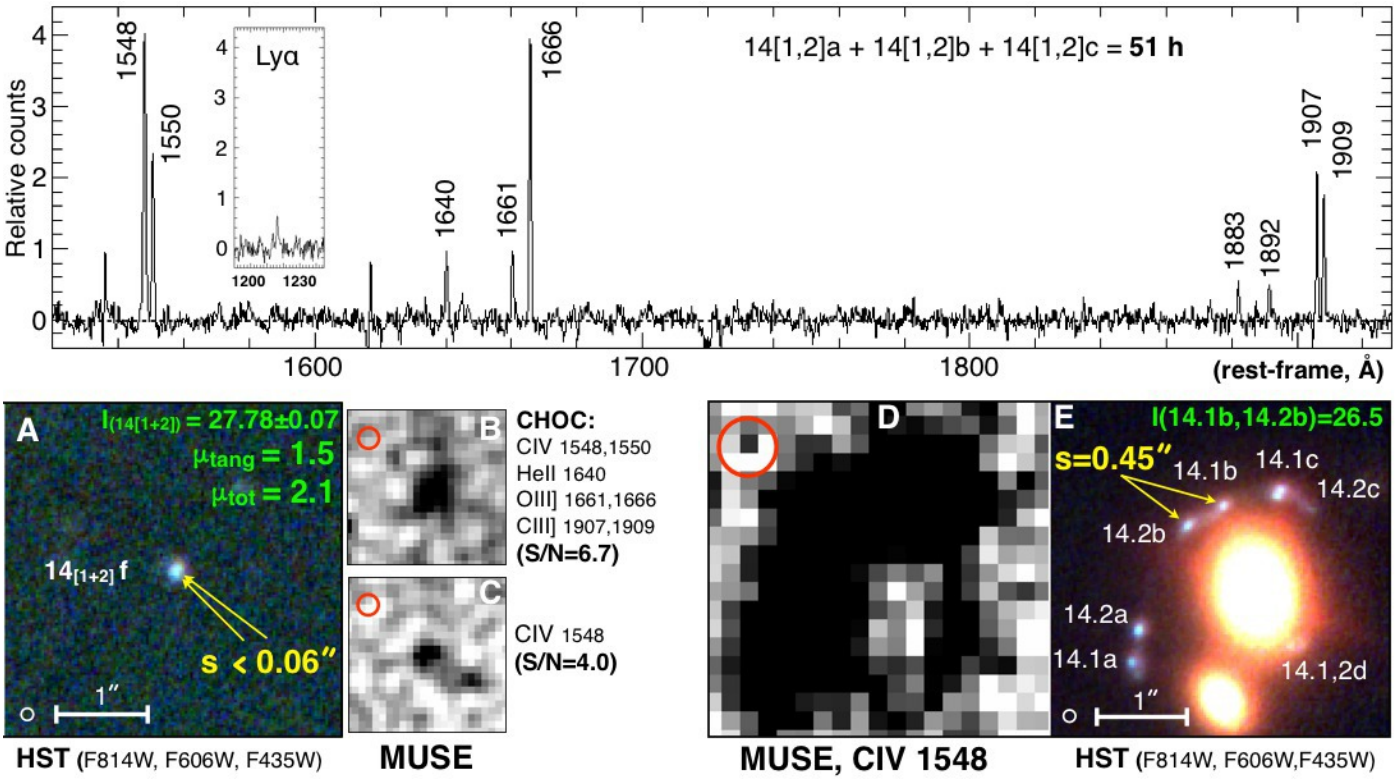

Fig. C.1. Revisited analysis of the double lensed source 14, made of a pair of knots, at the depth of MDLF. *Top panel*: continuum-subtracted one-dimensional spectrum of the pair obtained from the sum of the three multiple images 14a + 14b + 14c, equivalent to ≃51 h of integration. High-ionization lines are detected at $S/N \sim 10-50$, while the inset shows the deficient Lyα emission (the same scale on Y-axis is adopted), ∼8 times fainter than CIVλ1548, or ∼4 times fainter than CIII]λ1907. *Bottom-left panel A*: HST color image (red = $F105W$, green = $F814W$, blue = $F606W$) for the least magnified image (image $14_{[1+2]}$f), where the upper limit on the separation between knots 1 and 2 is quoted ($s < 0.06''$). *Panels B* and *C*: narrow-band (NB) continuum-subtracted MUSE images of the same $14_{[1+2]}$f, centered at the CIVλ1548 line and at the weight average of seven lines (the CHOC complex, see text for details). The NB images have been smoothed with a Gaussian kernel (σ = 1 pix). The red circles indicate the MUSE PSF of 0.″6. The same HST color image for the most magnified images 14.2b and 14.1b is shown in the *bottom-right E panel*, while the corresponding CIVλ1548 MUSE narrow-band image is in *panel D*. The small open white circle shown in the HST cutouts marks the $F814W$ PSF.

Appendix D: Spectral stacking

Section 5 presents the stacking of continuum-subtracted spectra and the detection maps (continuum-subtracted S/N spectra). We select here a sub-sample of sources in the redshift range of $2.9 < z < 3.4$ (14 entries, $\langle z \rangle = 3.2$) such that the complex of lines CIVλ1548, 1550, HeIIλ1640, OIII]λ1661, 1666, and CIII]$\lambda\lambda$1907, 1909 lies in the deeper wavelength interval probed by MUSE (6000−8300 Å, see Fig. 2), also avoiding the crowded region of intense sky lines ($\lambda > 8300$ Å). The spectra of the selected sample have integration time ranging from 17.1 to 51 h depending on the presence of (usable) multiple images. Figure D.1 shows individual and stacked spectra. Among the 14 sources with absolute magnitude ranging between −15.4 and −19 (with a median of −17.0), more than 50% show high-ionization lines with S/N ratios >3. Source 14 is the emitter with the most prominent lines detected with S/N ratio exceeding 50 (Figs. C.1 and D.1). The mean and median stacks show evident nebular emission lines, all of them well detected with $S/N > 10$.

The emission lines of the mean stack show values at the peak systematically higher than the median stack. The presence of source 14 with the highest S/N significantly affects the resulting average. This is shown in Fig. D.2 where the mean and median detection maps (i.e., stacked continuum-subtracted and inversely weighted by their errors) are shown for all sources ($2.9 < z < 3.4$, 14 entries) and after excluding only source 14. In the case where source 14 is excluded, the mean and median results are fully compatible, while the inclusion of source 14 boosts the mean. Overall, the presence of high-ionization lines detected on individual spectra and in the median stack (with or without source 14) show that at faint luminosity regimes ($-15 < M_{UV} < -18$), the occurrence of nebular high-ionization lines appears to be common.

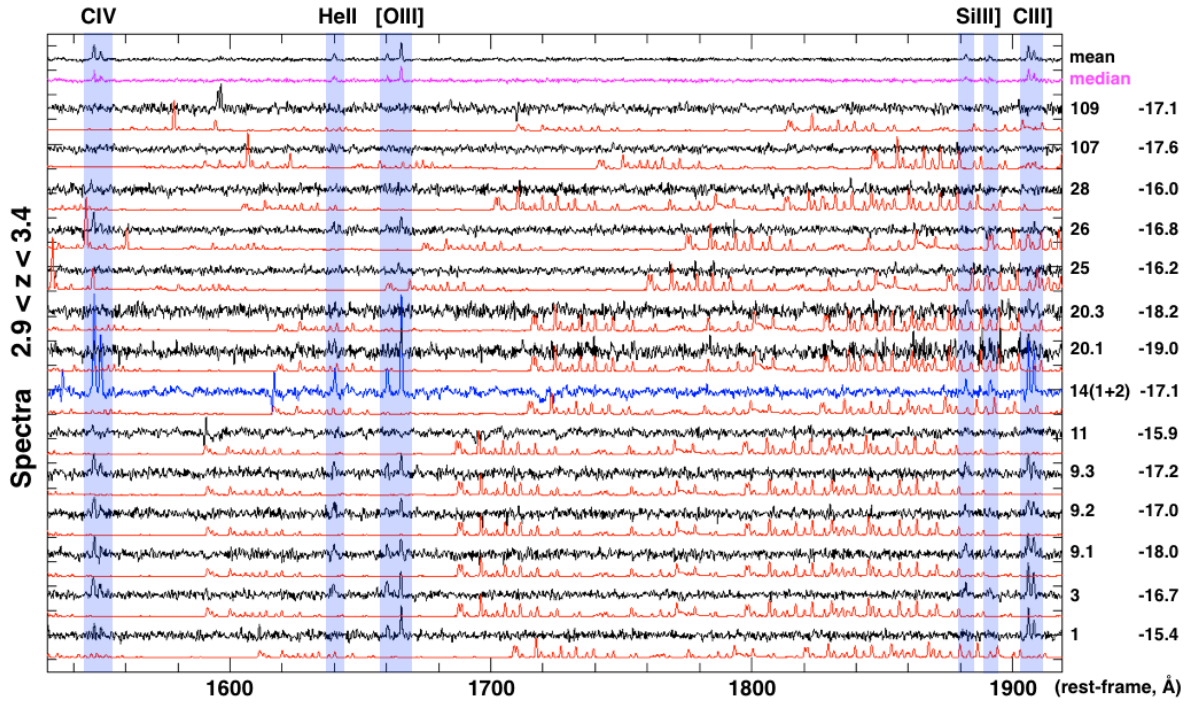

Fig. D.1. One-dimensional spectra (black lines) of a subset of sources with $2.9 < z < 3.4$ and average absolute magnitude $M_{\rm UV} = -17$, shown versus the rest-frame wavelength. Each spectrum is the weighted average of multiple images eventually producing net integration time of 17.1−51.3 h each. The ID and absolute magnitudes are reported on the rightmost two columns. The red lines show the error spectra associated to each spectrum, properly scaled and shifted for clarity below each black line. The red spectra show the pattern of the skylines. The blue spectrum indicates source 14, in which the high-ionization lines are prominently detected (see Fig. D.2 and relative caption for details). The two spectra on the *top panel* are the mean (black) and median (magenta) of the sample included in this figure. The vertical transparent stripes mark the location of the typical high-ionization lines (labeled on the top axis).

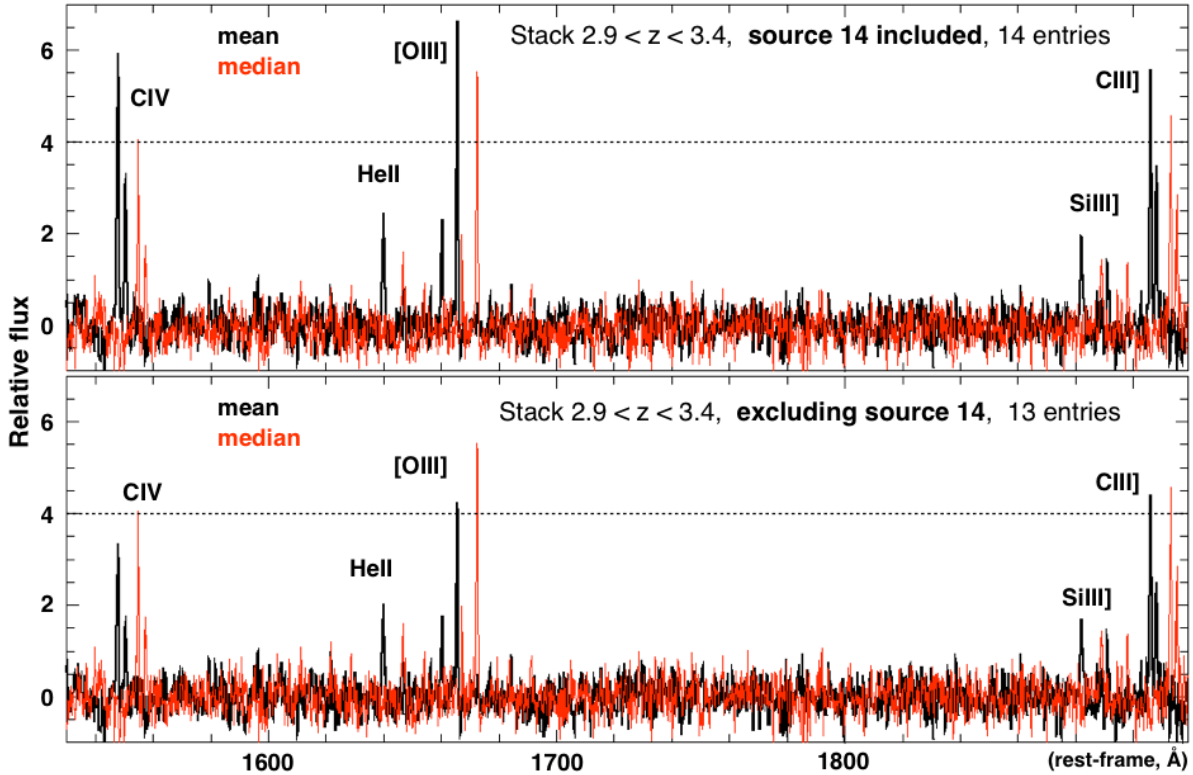

Fig. D.2. Mean (black line) and median (red line) stacked detection maps calculated from the set of spectra reported in Fig. D.1. The zoomed region including CIVλ1548, 1550, HeIIλ1640, OIII]λ1661, 1666, and CIII]$\lambda\lambda$1907, 1909 (*from left to right*) is shown. *Top panel*: all sources are included (14 entries), while in the *bottom panel* source 14 is excluded, that is the source showing prominent nebular high-ionization lines (see Fig. C.1, spectrum in blue; see also Fig. D.1). The median stacks (red lines) are rigidly redshifted by a fixed quantity for illustrative purposes only.

Appendix E: Magnification from relative flux ratios or angular separations: individual cases

We focus in this section on the magnification uncertainty of a subset of sources, specifically those discussed in the main text. Such analysis is not complete, however it is included here to describe a key method to overcome the large magnification uncertainty in the most magnified cases, where systematic uncertainties in the lens models may dominate. While statistical errors on magnifications have been discussed in Bergamini et al. (2021), a complementary and more robust method exploits flux ratios (or relative angular separations between clumps) among multiple images of the same family to estimate relative magnifications (Vanzella et al. 2016, 2017b). This is based on the following assumptions: (1) the multiple images do not cross or intercept the caustics on the source plane so that individual lensed images are produced, and (2) the images are well-detected and the inferred magnitudes free from significant contamination.

Such a magnification ratio can be rescaled to the magnification of the least magnified image, which typically has $\mu < 5$ and is far from the critical lines and, therefore, subject to small uncertainties from pure model prediction (<20%, Meneghetti et al. 2017). Under these conditions, the magnification of a lensed object subject to a complex geometry (e.g., close to the critical line) can be recovered with a relatively low uncertainty by propagating the error on μ of the least magnified image and the uncertainty associated to the photometry (flux ratios).

A challenging object discussed in this work is source 14 (see Sect. 6.2 and Appendix C), with magnification larger than 10 which arises from a complex lens geometry. In this case, the MDLF allowed us to confirm the redshift of the least magnified of the six multiple images, with $\mu = 2.08 \pm 0.02$, and to infer the magnification of the knots belonging to source 14 from the measured flux ratios based on HST photometry. Therefore, the total magnification can be estimated by rescaling the flux, while the tangential magnification can be estimated by rescaling the relative angular separation (see Appendix C). Table E.1 reports the results obtained from the application of this method, by comparing the magnification estimated directly from the lens model with the one derived using this method. The agreement in the case of source 14 is within 30% and in general within 50% ($\mu_{\rm tot-model}/\mu_{\rm tot-rescale} = 0.6 \div 1.5$). Among the sources presented in Table E.1, source 1 is a challenging case, for which this method does not work properly, since all three multiple images are highly magnified, including the least magnified (1a) with $\mu = 56.6 \pm 9.6$, due to its vicinity to the critical line. From pure flux rescaling the inferred μ(1c) is ∼500, while the lens model predicts $\mu(1c) = 78.1^{+19.1}_{13.4}$.

Apart from source 1, all the magnifications of the other sources reported in the table agree well with the model prediction, on average. However, in some cases such prediction are not within the formal 1-σ statistical error derived from the model (68% interval), suggesting that systematic errors can have a dominant role (e.g., Meneghetti et al. 2017). Despite of that, this preliminary test demonstrates the good predicting power of the lens model in the moderate-to-high magnification regime. Figure E.1 shows the HST RGB cutouts of the objects reported in Table E.1.

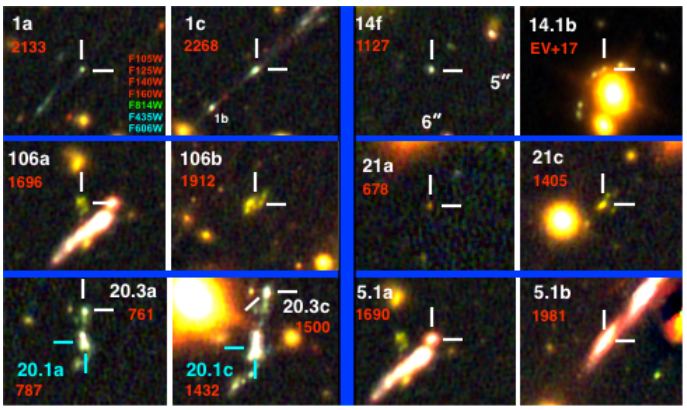

Fig. E.1. RGB HST images reported in Table E.1 are shown on two columns (divided by the vertical blue bar). The least magnified image of source 1 is shown on the *top-left* (1a), and the most magnified (1c) in the adjacent cutout on the *right*. The same applies for the other images. The size of the cutouts is $6'' \times 5''$. The ASTRODEEP identifier is quoted in red, while our internal ID is in white. For source 20 (*bottom-left*), two clumps are reported: 20.3a, 20.3c (marked with white segments), and 20.1a, 20.1c (cyan segments).

Table E.1. Comparison of magnification values from the method based on flux ratios (or clump angular separations) and from the lens model for a subset of sources discussed in the main text.

ID	z	Least μ ($\pm1\sigma$) [(#)]	Ratio [(⋆)]	Rescaled μ ($\pm1\sigma$)	Model μ^{+}_{-}68 (95,99)%	Sect./Fig.
1c [(I)]	3.2370	$\mu_{\rm tot}$(1a) = 56.6 ± 9.6	8.89 ± 1.86 (F)	$\mu_{\rm tot}$ = 502 ± 136	$\mu_{\rm tot} = 78.1^{+19.1\,(34.9,59.9)}_{-13.4\,(20.4,26.1)}$	6.1/16, 14
5.1b	1.8961	$\mu_{\rm tot}$(5.1a) = 3.63 ± 0.09	4.33 ± 0.13 (F)	$\mu_{\rm tot}$ = 15.7 ± 0.6	$\mu_{\rm tot} = 9.1^{+0.6\,(1.2,2.0)}_{-0.6\,(0.9,1.1)}$	3/5
5.[4,2)]c [(II)]	1.8961	$\mu_{\rm tang}$(5.(4, 2)a) = 2.4 ± 0.1	3.07 ± 0.36 (A)	$\mu_{\rm tang}$ = 7.5 ± 0.9	$\mu_{\rm tang}$ = 5−9	3/5
14.1b [(III)]	3.2226	$\mu_{\rm tot}$(14f) = 2.08 ± 0.02	7.29 ± 0.83 (F)	$\mu_{\rm tot}$ = 15.2 ± 1.7	$\mu_{\rm tot} = 19.4^{+11.1\,(29.6,69.6)}_{-5.9\,(8.1,9.4)}$	6.2/16, C.1
14.[1,2]b [(IV)]	3.2226	$\mu_{\rm tang}$(14f) = 1.5 ± 0.1	>7.5 (A)	$\mu_{\rm T}$ > 11.2	$\mu_{\rm T} \simeq 7-20$	6.2/16, C.1
20.3c	3.2190	$\mu_{\rm tot}$(20.3a) = 2.24 ± 0.03	2.97 ± 0.22 (F)	$\mu_{\rm tot}$ = 6.7 ± 0.5	$\mu_{\rm tot} = 5.0^{+0.1\,(0.2,0.3)}_{-0.1\,(0.2,0.3)}$	3/9
20.1c	3.2190	$\mu_{\rm tot}$(20.1a) = 2.20 ± 0.03	3.47 ± 0.14 (F)	$\mu_{\rm tot}$ = 7.6 ± 0.4	$\mu_{\rm tot} = 6.2^{+0.2\,(0.3,0.5)}_{-0.2\,(0.3,0.4)}$	3/9
21c [(II)]	5.1093	$\mu_{\rm tot}$(21a) = 2.04 ± 0.02	7.49 ± 0.84 (F)	$\mu_{\rm tot}$ = 15.3 ± 1.7	$\mu_{\rm tot} = 11.6^{+0.3\,(0.6,0.8)}_{-0.3\,(0.5,0.6)}$	3/B.1
106b	4.1162	$\mu_{\rm tot}$(106a) = 4.54 ± 0.11	1.77 ± 0.11 (F)	$\mu_{\rm tot}$ = 8.1 ± 0.5	$\mu_{\rm tot} = 11.8^{+0.6\,(1.2,1.8)}_{-0.5\,(0.8,1.3)}$	3/7

Notes. [(#)]The magnification value of the least magnified multiple image. [(⋆)]Flux or angular separation ratios are indicated with "F" or "A", respectively, and are calculated on images with IDs reported in Cols. 1 and 3. [(I)]The flux ratio calculated among images 1a (the least magnified) and 1c (the most magnified), based on the $F814W$ band. We note that $\mu_{\rm tot}$(1a) is possibly subjected to large uncertainty, we rely on the lens model for the magnification of this object (see Appendix E). [(II)]Ratio of the angular separations between knots 5.4 and 5.2 for group images "a" and "c". [(III)]Based on flux ratio between images 14.2b (or 14.1b), and the least magnified image 14f, taking into account that 14f is the sum of the two knots (14.1+14.2, see Sect. 6.2). [(IV)]Based on the relative angular separation among knots 14.2b−14.1b and the upper limit on 14.1f (see Appendix C).